Research Square

Preprints are preliminary reports that have not undergone peer review.
They should not be considered conclusive, used to inform clinical practice,
or referenced by the media as validated information.

# Interface Engineering for Substantial Performance Enhancement in Epitaxial All Perovskite Oxide Capacitor

**Youngsung Kim** ( kimyongsung@samsung.com )
Samsung Advanced Institute of Technology
**Jeongil Bang**
Samsung Advanced Institute of Technology
**Jaeho Lee**
Samsung Advanced Institute of Technology
**Eun Cheol Do**
Samsung Advanced Institute of Technology
**Hyungjun Kim**
Samsung Advanced Institute of Technology
**Byunghoon Na**
Samsung Advanced Institute of Technology
**Haeryong Kim**
Samsung Advanced Institute of Technology
**Bo-Eun Park**
Samsung Advanced Institute of Technology
**Jooho lee**
Samsung (South Korea)
**Che-Heung Kim**
Samsung Advanced Institute of Technology
**Ho Won Jang**
Seoul National University https://orcid.org/0000-0002-6952-7359

**Article**

**Keywords:** perovskite oxide, capacitor, interface engineering, epitaxial, dielectrics

**Posted Date:** August 16th, 2022

**DOI:** https://doi.org/10.21203/rs.3.rs-1911322/v1

**License:** This work is licensed under a Creative Commons Attribution 4.0 International License.
Read Full License

**Version of Record:** A version of this preprint was published at NPG Asia Materials on January 27th, 2023. See the published version at https://doi.org/10.1038/s41427-022-00460-x.

# Abstract

Capacitors based on $ABO_3$-type perovskite oxides show considerable promise for overcoming the limitations of nanoscale integration for dynamic random access memory (DRAM) devices. Among thermodynamically stable perovskite oxides, titanates ($ATiO_3$) exhibit high dielectric permittivity in metal–insulator–metal (MIM) configurations. However, their ultimate properties remain under scrutiny for mitigating the large leakage current caused by their narrow bandgap (3 eV). Herein, substantially enhanced dielectric properties of an epitaxial $SrRuO_3/Ba_{0.5}Sr_{0.5}TiO_3/SrRuO_3$ MIM capacitor with a thin dielectric layer (10 nm) are reported. The dielectric/electrode heterointerface was engineered to realize a capacitor with low leakage current and high dielectric permittivity. A pit-free and stoichiometric $SrRuO_3$ bottom electrode with atomically smooth surface was exploited for suppressing defect formation at the heterointerface. The critical roles of oxygen vacancies and substituted transition-metal atoms in determining the leakage current were accessed and a strategy for reducing the leakage current *via* interface engineering was established. Consequently, a dielectric permittivity of 861 and leakage current density of $5.15 \times 10^{-6}$ A/cm$^2$ at 1 V were obtained with the thinnest dielectric layer ever reported. Our work paves the way for the development of perovskite-oxide-based capacitors in next-generation DRAM memories.


# Introductions

Dynamic random access memory (DRAM) operation requires a certain level of charge-storage capability. With developments in DRAM generation, the thickness of capacitors should decrease to satisfy the high-aspect-ratio requirement established by the design rule of DRAM capacitors. However, this scaling down of capacitors limits their charge-storage capability. Therefore, the properties of the thin dielectric layer must be enhanced and optimized.[1,2]

To overcome these problems, investigations on metal–insulator–metal (MIM) capacitors must be conducted to leverage their high dielectric permittivity ($\kappa$) values and thin dielectric layers. Because increasing the permittivity of the dielectric in ultrathin capacitors can offset the aforementioned charge-storage limitations, ternary perovskite oxides that exhibit higher dielectric permittivity values than that of $ZrO_2$ and $HfO_2$, which are currently used in DRAM capacitors, have attracted research attention. In particular, $SrTiO_3$ and doped $SrTiO_3$ are representative ternary-perovskite-oxide materials; $SrTiO_3$ exhibits general dielectric characteristics, whereas Ba-doped $SrTiO_3$—a representative relaxor-ferroelectric material—shows extremely high dielectric permittivity at the ferroelectric-to-paraelectric transition temperature. SrTiO3 shows paraelectric property and has no temperature which shows transition of dielectric property. However, Ba-doped SrTiO3 substituted with Ba instead of some Sr at the A-site of SrTiO3 shows ferroelectric-to-paraelectric transition. And the transition temperature increases with increasing amount of doped Ba. Therefore, a high dielectric permittivity of Ba-doped $SrTiO_3$ can be achieved at a desired temperature by controlling the Ba concentration.[3–5]

In the dielectric layer, carriers can be transferred *via* two mechanisms: material-property-induced and defect-induced carrier conduction. Material-property-induced carrier conduction includes Schottky emission and direct tunneling, which occur when the bandgap of the dielectric is narrow, and when the dielectric is extremely thin, respectively. Defect-induced carrier conduction includes Poole–Frenkel (P–F) emission and hopping conduction, which are caused by defects acting as trap sites in the dielectric layer. Both the mechanisms, which are caused by material properties and defects in the dielectric layer, affect its leakage current and are simultaneously activated. Therefore, as the thickness of $SrTiO_3$ or Ba-doped $SrTiO_3$ with a narrow bandgap (3 eV) decreases, the defects in the dielectric layer increase the leakage current and suppress the ultimate dielectric properties. To overcome these limitations concerning the leakage current in Ba-doped $SrTiO_3$, investigations on realizing high-performance capacitors with defect control *via* interface engineering must be prioritized.[6–8]

In this study, the leakage behavior and defect-formation mechanism of an $SrRuO_3/Ba_{0.5}Sr_{0.5}TiO_3/SrRuO_3$ capacitor were investigated through precisely controlled interfacial engineering using an ultrathin epitaxial scheme to fabricate a 10-nm-thick dielectric layer.

# Materials And Methods

**Thin film growth.** All the perovskite oxide layers were grown by pulsed laser deposition (PLD) using a KrF excimer laser (λ = 248 nm). Prior to the film growth, an $SrTiO_3$ (100) single-crystal substrate was etched using a buffered hydrofluoric acid etchant and annealed at 1000°C for 1 h to form a Ti-terminated surface. $SrRuO_3$ and $Ba_{0.5}Sr_{0.5}TiO_3$ perovskite oxides were grown in an oxygen atmosphere at a working pressure of 100 mTorr. During the PLD, the substrate temperature was maintained at 700°C. The thicknesses of the bottom electrode, dielectric layer, and top electrode were fixed at 30, 10, and 50 nm, respectively. To engineer the interface between the bottom electrode and dielectric layer, $SrRuO_3$ bottom electrodes were grown at repetition frequencies of 2, 5, and 10 Hz. Subsequently, the $Ba_{0.5}Sr_{0.5}TiO_3$ dielectric layer and $SrRuO_3$ top electrode were grown at an identical frequency of 10 Hz.

**Structural and electrical characterization.** AFM, XRD, and the Van der Pauw method were employed to confirm that the $SrRuO_3$ bottom electrodes fabricated at the different repetition frequencies were of high quality. The microstructure of the epitaxially grown $SrRuO_3/Ba_{0.5}Sr_{0.5}TiO_3/SrRuO_3$ capacitor was characterized by cross-sectional HAADF-STEM. The engineered interface between the $SrRuO_3$ bottom electrode and $Ba_{0.5}Sr_{0.5}TiO_3$ was analyzed by HAADF intensity profiling. All the top $SrRuO_3$ electrodes were defined by patterning with a Ti/Pt hard mask. The temperature-dependent *C*–*V* and *I*–*V* characteristics were determined using a probe station with a grounded bottom electrode and biased top electrode.

**Band structure predictions.** Density functional theory (DFT) calculations were performed using the Vienna *ab initio* simulation package (VASP) based on the projector augmented wave (PAW)[29–32] method with the Perdew–Burke–Ernzerhof (PBE) exchange-correlation functional. An energy cutoff of 600 eV was used to

truncate the plane wave basis. Crystal structures were fully relaxed (with a force convergence criterion of 0.001 eV/Å) unless otherwise stated.

# Results And Discussion

The relaxor-ferroelectric $SrRuO_3/Ba_{0.5}Sr_0.5TiO3/SrRuO_3$ capacitor was epitaxially fabricated by pulsed laser deposition (PLD). To control the electrode–dielectric interface, epitaxial $SrRuO_3$ bottom electrodes were grown at different laser repetition frequencies (10, 5, and 2 Hz). Figure 1a–c shows the surface morphologies of these $SrRuO_3$ bottom electrodes, which were imaged by atomic force microscopy (AFM). These results indicated that the $SrRuO_3$ deposited at a repetition frequency of 10 Hz had pits with a half-unit-cell depth (~ 0.2nm) on the surface, which disappeared when the repetition frequency was lowered to 2 Hz. These phenomena readily occur when epitaxial $SrRuO_3$ films are grown by PLD. At high repetition frequencies, each $SrRuO_3$ adatom collides with its adjacent adatom prior to its kinetic stabilization at the edge of the substrate terrace. This collision generates a volatile $RuO_4$ phase and pits on the film surface. Because of these phenomena, epitaxial $SrRuO_3$ films fabricated at high repetition frequencies have a Ru-deficient stoichiometric property.[9] The Ru/Sr ratios of the $SrRuO_3$ films were determined with respect to the repetition frequency by obtaining Ru-3d core-level X-ray photoelectron spectroscopy (XPS) profiles, and compared with that of $SrRuO_3$ target which is used in growth. (Figure S1). Similarly, the Ru-deficient stoichiometric property was estimated by obtaining X-ray diffraction (XRD) patterns and resistivity–temperature data (Fig. 1d and 1e, respectively). When $SrRuO_3$ has Ru-deficient stoichiometry, it shows an orthorhombic-to-tetragonal phase transition at the critical point. The *c*-axis of $SrRuO_3$ is consequently lengthened and manifests as an XRD peak that shifts to lower angles without deterioration of crystallinity (Fig. 1d).[10–12] Moreover, Ru-deficient $SrRuO_3$ is known to exhibit a higher resistivity and lower Curie temperature than those of stoichiometric $SrRuO_3$.[13,14] Therefore, an $SrRuO_3$ bottom electrode with a well-arranged and pit-free surface was obtained at a low PLD repetition frequency for operating as the bottom of the electrode–dielectric interface.

To clarify the effects of interface engineering of the MIM capacitor, the $Ba_{0.5}Sr_{0.5}TiO_3$ dielectric and $SrRuO_3$ top electrodes were grown under identical conditions at the repetition frequencies of the $SrRuO_3$ bottom electrode. Figure 2a,b; 2c,d; and 2e,f show cross-sectional scanning transmission electron microscopy (STEM) images of the MIM capacitors and the high-angle annular dark-field (HAADF) intensity profiles of the bottom-electrode–dielectric interface with $SrRuO_3$ bottom electrodes fabricated at 2, 5, and 10 Hz, respectively. The peak intensities of the HAADF profiles extracted from sites A and B of perovskite structure were plotted (Fig. 2g,h). As shown in the cross-sectional STEM and fast Fourier transform (FFT) images (Fig. 2a, 2c, and 2e), all films were epitaxially grown without any noticeable differences. However, differences were observed for the $Ba_{0.5}Sr_{0.5}TiO_3$ films with the bottom electrodes in the HAADF intensity profiles of B-site atoms (Fig. 2h). In the case of $Ba_{0.5}Sr_{0.5}TiO_3$ grown on $SrRuO_3$ at a laser frequency of 10 Hz, the HAADF intensity of the B-site formed a slope that was three-unit-cell sized; no changes were observed in the A-site intensities. The extent of this slope decreased to one or two unit

cells at the interface between $Ba_{0.5}Sr_{0.5}TiO_3$ and the 5-Hz-grown bottom $SrRuO_3$ electrode, and disappeared at the interface between $Ba_{0.5}Sr_{0.5}TiO_3$ and the 2-Hz-grown $SrRuO_3$ (Fig. 2g,h). This slope was presumably formed by the half-unit-cell deep pits on the surface of $SrRuO_3$ (Fig. 1a–c). During the growth of $Ba_{0.5}Sr_{0.5}TiO_3$, interdiffusion can occur between pits with high surface energy. Certain atoms from the bottom $SrRuO_3$ layer, especially B-site Ru, can diffuse to the $Ba_{0.5}Sr_{0.5}TiO_3$ layer.

The dielectric properties of the capacitors were determined with respect to the repetition frequency of the $SrRuO_3$ bottom electrodes (Fig. 3). Although the maximum value of dielectric permittivity ($\kappa_{max}$) slightly decreased from 931 to 861 as the repetition frequency of the bottom $SrRuO_3$ electrode decreased from 10 to 2 Hz, the dissipation factors at both positive and negative voltages were suppressed by more than one order of magnitude (Fig. 3a). Additionally, as the repetition frequency of the bottom $SrRuO_3$ electrode decreased, the leakage current density was dramatically suppressed (Fig. 3b); the leakage current density at a bias of 1 V ($J$@1V) decreased from $4.28 \times 10^{-2}$ to $5.15 \times 10^{-6}$ A/cm$^2$.

The slight decrease in dielectric permittivity with decreasing laser repetition frequency of the bottom electrode can be explained by the HAADF intensity profiles shown in Fig. 2. The effective thickness of $Ba_{0.5}Sr_{0.5}TiO_3$ on 5 and 10 Hz of $SrRuO_3$ decreased owing to the Ru diffusion at the interface. Therefore, the dielectric permittivity, which was calculated based on the 10-nm-thick $Ba_{0.5}Sr_{0.5}TiO_3$ dielectric layer, increased in proportion to the decrease in effective thickness of $Ba_{0.5}Sr_{0.5}TiO_3$.

To clarify the four-order-of-magnitude suppression of the leakage current *via* interface engineering, first, the work functions of $SrRuO_3$ were determined according to the repetition frequency by ultraviolet photoelectron spectroscopy (UPS) to distinguish the material-induced and defect-induced conduction mechanisms (Figure S2). All the $SrRuO_3$ films exhibited identical work functions of 5.1 eV, which indicated that the material-induced conduction, especially Schottky emission, could be excluded. Next, to reveal the specific mechanism under defect-induced conduction, current–voltage characteristics were determined at different temperatures (Fig. 3c). The obtained fits indicated that hopping conduction occurred in the MIM capacitor with the 2-Hz-grown $SrRuO_3$, whereas P–F emission occurred in the capacitors with 5- and 10-Hz-grown $SrRuO_3$. The current density induced by these conduction mechanisms can be expressed by following equations:

$$J_{hopping} = qanv \cdot exp\left[\frac{qaE}{kT} - \frac{q\varphi_T}{kT}\right], \quad (1)$$

$$J_{P-F} = q\mu N_c E \cdot exp\left[\frac{-q(\varphi_T - \sqrt{qE/\pi\varepsilon_r\varepsilon_0}}{kT}\right], \quad (2)$$

where $q$ is the charge of an electron, $a$ is the hopping distance, $n$ is the electron concentration in the conduction band, $v$ is the thermal vibration frequency of electrons at trap sites, E is the applied electrical

field, $q\varphi_T$ is the trap energy level, which refers to the activation energy of trapped electrons, μ is the electronic drift mobility, and $N_c$ is the density of states (DOS) in the conduction band. [15] Using these equations and the data-fitting results, the energy level of defects in $Ba_{0.5}Sr_{0.5}TiO_3$ for the different $SrRuO_3$ growth conditions were calculated (Table S1). The shallow defects formed on the rough surface of the $SrRuO_3$ bottom electrodes presumably act as trap sites for P–F emission, indicating that the major defects in the $Ba_{0.5}Sr_{0.5}TiO_3$ dielectric layer can be altered by changing the surface morphology of the bottom electrode.

To determine the defects at each energy level, DOS data were acquired using 3 × 3 × 3 supercells with five different configurations (Fig. 4f–j). The corresponding structures of the $SrTiO_3$-based supercells modeled with Ru substitution and oxygen vacancies are shown in Fig. 4a–e. Ti-3d and O-2p orbitals are known to form conduction and valance bands in $SrTiO_3$, respectively. Moreover, in case oxygen vacancies are present in $SrTiO_3$, two Ti-3d orbitals adjacent to an oxygen vacancy and O-2p orbitals adjacent to each Ti-3d orbital next to the oxygen vacancy form a hybrid orbital, which exhibits in-gap states of 0.7 eV in the bandgap of $SrTiO_3$.[16] The calculation results (Fig. 4f,g) are in good agreement with the observations from these previous studies. In case a ruthenium atom substitutes a B-site Ti atom, in-gap states that have deep levels similar to those of oxygen vacancies are formed, and these in-gap states consist of Ti-d, O-p, and Ru-d orbitals (Fig. 4h). When the substituted Ru atom and oxygen vacancy are separated by a significant distance, deep in-gap states are formed in the $SrTiO_3$ bandgap (Fig. 4i). Additionally, in case the oxygen vacancy is adjacent to the substituted Ru and the effects of the oxygen vacancy and substituted Ru on changes in the DOS are correlated, a shallow in-gap state is generated just below the conduction band (Fig. 4j). Therefore, the data fitting based on the conduction mechanism and the DOS calculation reveal that the orbital interaction between the substituted Ru and oxygen vacancy generates shallow in-gap states, which can act as trap sites for P–F emission at MIM capacitor with 5- and 10-Hz grown $SrRuO_3$ electrode.

The electrical properties of capacitors fabricated in this study were plotted on a 3D graph featuring the following parameters: dielectric film thickness ($t_d$), equivalent oxide thickness (*EOT*) which is representative parameter indicating dielectric efficiency reflecting the thickness of dielectric layer, and leakage current density (*J*); moreover, these data were compared with those of previous studies (Fig. 5). The electrical properties of previously reported capacitors with the $SrRuO_3$ bottom electrode were specifically compared.[17–28] High-performance capacitors with thinner dielectric layers tend to exhibit lower *EOT* and *J* values. With respect to the *EOT* distribution according to the thickness of the dielectric layer (Fig. 5a), the interface-engineered capacitor with the $SrRuO_3$ bottom electrode grown at 2 Hz exhibited an excellent *EOT* despite having a thinner dielectric layer than that in previously reported capacitors. Moreover, with respect to the $J–t_d$ distribution (Fig. 5b), the interface engineering performed in this study yielded *J* values equivalent to those of previously reported capacitors but at a lower dielectric-layer thickness. Additionally, in the *EOT*–*J* plot (Fig. 5c), which is typically used to compare the

performance of capacitors, the results obtained in this study suggest that a higher performance than that of previously reported devices was achieved.

# Conclusions

Interface engineering of epitaxially grown $SrRuO_3/Ba_{0.5}Sr_{0.5}TiO_3/SrRuO_3$ capacitors was performed to realize a high-performance capacitor containing a thin dielectric layer with high dielectric permittivity and low leakage current. The bottom-electrode/dielectric-layer interface was controlled using the laser repetition frequency of PLD. A pit-free interface, which was formed by interface engineering at a low laser-repetition frequency, stabilized the Ru atoms in $SrRuO_3$, which essentially hindered their diffusion from $SrRuO_3$ to $Ba_{0.5}Sr_{0.5}TiO_3$, unlike in the case of $SrRuO_3$ with pits on its surface. The interactions between Ru atoms and oxygen vacancies in the dielectric layer were found to possibly form a shallow in-gap state, which likely acted as the trap site for P–F emission. The engineering of the interface between the bottom $SrRuO_3$ electrode and $Ba_{0.5}Sr_{0.5}TiO_3$ dielectric layer evidently minimized the formation of trap sites and suppressed the leakage current of the capacitor without a large decrease in dielectric permittivity. The estimated dielectric permittivity (861) and leakage current density ($5.15 \times 10^{-6}$ A/cm$^2$) at 1 V of the 10-nm-thick dielectric layer indicate that a high $\kappa$ and low leakage current were simultaneously achieved with the thinnest dielectric layer ever reported. Additionally, this strategy provides clues to facilitate nanoscale integration of DRAM devices.

# Declarations

ACKNOWLEDGMENT

This research was supported by Samsung Advanced Institute of Technology (SAIT).

CONFLICTS OF INTERESTS

This manuscript has not been published or presented elsewhere in part or in entirety and is not under consideration by another journal. We have read and understood your journal’s policies, and we believe that neither the manuscript nor the study violates any of these. There are no conflicts of interest to declare.

# References

1. Dagdeviren, C., et al. Conformable Amplified Lead Zirconate Titanate Sensors with Enhanced Piezoelectric Response for Cutaneous Pressure Monitoring. Nat. Commun. **5**, 4496 (2014).
2. Damjanovic, D. Ferroelectric, Dielectric and Piezoelectric Properties of Ferroelectric Thin Films and Ceramics. Rep. Prog. Phys. **61**, 1267 (1998).
3. Ma, W., Cross, L. E. Flexoelectric Polarization of Barium Strontium Titanate in the Paraelectric State. Appl. Phys. Lett. **81**, 3440–3442 (2002).

4. Jeon, J.-H. Effect of $SrTiO_3$ Concentration and Sintering Temperature on Microstructure and Dielectric Constant of $Ba_{1-x}Sr_xTiO_3$. J. Eur. Ceram. Soc. **24**, 1045–1048 (2004).
5. Garten, L. M., et al. Trolier-McKinstry, S. Relaxor Ferroelectric Behavior in Barium Strontium Titanate. J. Am. Ceram. Soc. **99**, 1645–1650 (2016).
6. Vehkamäki, M., Hatanpää, T., Hänninen, T., Ritala, M., Leskelä, M. Growth of $SrTiO_3$ and $BaTiO_3$ Thin Films by Atomic Layer Deposition. Electrochem. Solid-State Lett. **2**, 504 (1999).
7. Kim, S. K., et al. Capacitors with an Equivalent Oxide Thickness of < 0.5 nm for Nanoscale Electronic Semiconductor Memory. Adv. Funct. Mater. **20**, 2989–3003 (2010).
8. Hou, C., et al. Ultrahigh Energy Density in $SrTiO_3$ Film Capacitors. ACS Appl. Mater. Interfaces. **9**, 20484–20490 (2017).
9. Schraknepper, H., Bäumer, C., Gunkel, F., Dittmann, R., De Souza, R. A. Pulsed Laser Deposition of $SrRuO_3$ Thin-Films: The Role of the Pulse Repetition Rate. APL Mater. **4**, 126109 (2016).
10. Anooz, S. B., et al. Structural and Transport Properties of $SrRuO_3$ Thin Films Grown by MOCVD on (001) $SrTiO_3$ Substrates: The Role of Built-in Strain and Extra Phases. Mater. Sci. Eng., B. **176**, 647–652 (2011).
11. Maria, J. P., Trolier-McKinstry, S., Schlom, D. G., Hawley, M. E., Brown, G. W. The Influence of Energetic Bombardment on the Structure and Properties of Epitaxial $SrRuO_3$ Thin Films Grown by Pulsed Laser Deposition. J. Appl. Phys. **83**, 4373–4379 (1998).
12. Chen, C. L., et al. Epitaxial $SrRuO_3$ Thin Films on (001) $SrTiO_3$. Appl. Phys. Lett. **71**, 1047–1049 (1997).
13. Siemons, W., et al. Dependence of the Electronic Structure of $SrRuO_3$ and Its Degree of Correlation on Cation Off-Stoichiometry. Phys. Rev. B. **76**, 075126 (2007).
14. Lee, S. A., et al. Enhanced Electrocatalytic Activity *via* Phase Transitions in Strongly Correlated $SrRuO_3$ Thin Films. Energy Environ. Sci. **10**, 924–930 (2017).
15. Chiu, F.-C. A Review on Conduction Mechanisms in Dielectric Films. *Adv. Mater. Sci. Eng.* 2014, 578168 (2014).
16. Lin, C., Demkov, A. A. Electron Correlation in Oxygen Vacancy in $SrTiO_3$. Phys. Rev. Lett. **111**, 217601 (2013).
17. Pintilie, L., Vrejoiu, I., Hesse, D., LeRhun, G., Alexe, M. Ferroelectric Polarization-Leakage Current Relation in High Quality Epitaxial Pb(Zr, Ti)$O_3$ Films. Phys. Rev. B. **75**, 104103 (2007).
18. Sharma, A. P., Pradhan, D. K., Pradhan, S. K., Bahoura, M. Large Energy Storage Density Performance of Epitaxial BCT/BZT Heterostructures *via* Interface Engineering. Sci. Rep. **9**, 16809 (2019).
19. Zhang, W., et al. Space-Charge Dominated Epitaxial $BaTiO_3$ Heterostructures. Acta Mater. **85**, 207–215 (2015).
20. Ventura, J., et al. Structural and Dielectric Properties of (001) and (111)-Oriented $BaZr_{0.2}Ti_{0.8}O_3$ Epitaxial Thin Films. Thin Solid Films. **518**, 4692–4695 (2010).

21. Lee, J.-S., Li, Y., Lin, Y., Lee, S. Y., Jia, Q. X. Hydrogen-Induced Degradation in Epitaxial and Polycrystalline (Ba,Sr)$TiO_3$ Thin Films. Appl. Phys. Lett. **84**, 3825–3827 (2004).
22. Zhu, X., Zheng, D., Peng, W., Miao, J., Li, J. Structural and Electrical Properties of Epitaxial $Ba_{0.5}Sr_{0.5}TiO_3/SrRuO_3$ Heterostructures Grown by Pulsed Laser Deposition. J. Cryst. Growth. **268**, 192–197 (2004).
23. Abazari, M., Akdoğan, E. K., Safari, A. Effect of Manganese Doping on Remnant Polarization and Leakage Current in $(K_{0.44}, Na_{0.52}, Li_{0.04})(Nb_{0.84}, Ta_{0.10}, Sb_{0.06})O_3$ Epitaxial Thin Films on $SrTiO_3$. Appl. Phys. Lett. **92**, 212903 (2008).
24. Liang, Y.-C., Liang, Y.-C. Fabrication and Electrical Properties of Strain-Modulated Epitaxial $Ba_{0.5}Sr_{0.5}TiO_3$ Thin-Film Capacitors. J. Electrochem. Soc. **154**, G193 (2007).
25. Acharya, M., et al. Exploring the $Pb_{1-x}Sr_xHfO_3$ System and Potential for High Capacitive Energy Storage Density and Efficiency. Adv. Mater. **34**, 2105967 (2022).
26. Gao, D., et al. All-Inorganic Flexible $Ba_{0.67}Sr_{0.33}TiO_3$ Thin Films with Excellent Dielectric Properties over a Wide Range of Frequencies. ACS Appl. Mater. Interfaces. **11**, 27088–27097 (2019).
27. Miura, H., Kumagai, Y., Fujisaki, Y. Hillock Growth at the Surface of Pt/TiN Electrodes for Ferroelectric Capacitors During Annealing in $N_2/O_2$ Ambient. In *MRS Online Proceedings Library (OPL), Volume 493: Symposium U – Ferroelectric Thin Film VI*, Materials Research Society, p 137 (1997).
28. Dittmann, R., et al. Sharp Ferroelectric Phase Transition in Strained Single-Crystalline $SrRuO_3/Ba_{0.7}Sr_{0.3}TiO_3/SrRuO_3$ Capacitors. Appl. Phys. Lett. **83**, 5011–5013 (2003).
29. Kresse, G., Hafner, J. Ab Initio Molecular Dynamics for Liquid Metals. Phys. Rev. B. **47**, 558 (1993).
30. Kresse, G., Furthmüller, J. Efficiency of Ab-Initio Total Energy Calculations for Metals and Semiconductors Using a Plane-Wave Basis Set. Comput. Mater. Sci. **6**, 15–50 (1996).
31. Kresse, G., Furthmüller, J. Efficient Iterative Schemes for Ab Initio Total-Energy Calculations Using a Plane-Wave Basis Set. Phys. Rev. B. **54**, 11169 (1996).
32. Kresse, G., Joubert, D. From Ultrasoft Pseudopotentials to the Projector Augmented-Wave Method. Phys. Rev. B. **59**, 1758 (1999).
33. Sampath Kumar, V., Niranjan, M. K. Effect of Surface Structure on Workfunction and Schottky-Barrier Height in $SrRuO_3/SrTiO_3$ (001) Heterojunctions. J. Appl. Phys. **115**, 173705 (2014).
34. Jacobs, R., Booske, J., Morgan, D. Understanding and Controlling the Work Function of Perovskite Oxides Using Density Functional Theory. Adv. Funct. Mater. **26**, 5471–5482 (2016).
35. Mitra, C., Lin, C., Robertson, J., Demkov, A. A. Electronic Structure of Oxygen Vacancies in $SrTiO_3$ and $LaAlO_3$. Phys. Rev. B. **86**, 155105 (2012).
36. Lopez-Bezanilla, A., Ganesh, P., Littlewood, P. B. Magnetism and Metal-Insulator Transition in Oxygen-Deficient $SrTiO_3$. Phys. Rev. B. **92**, 115112 (2015).

# Figures

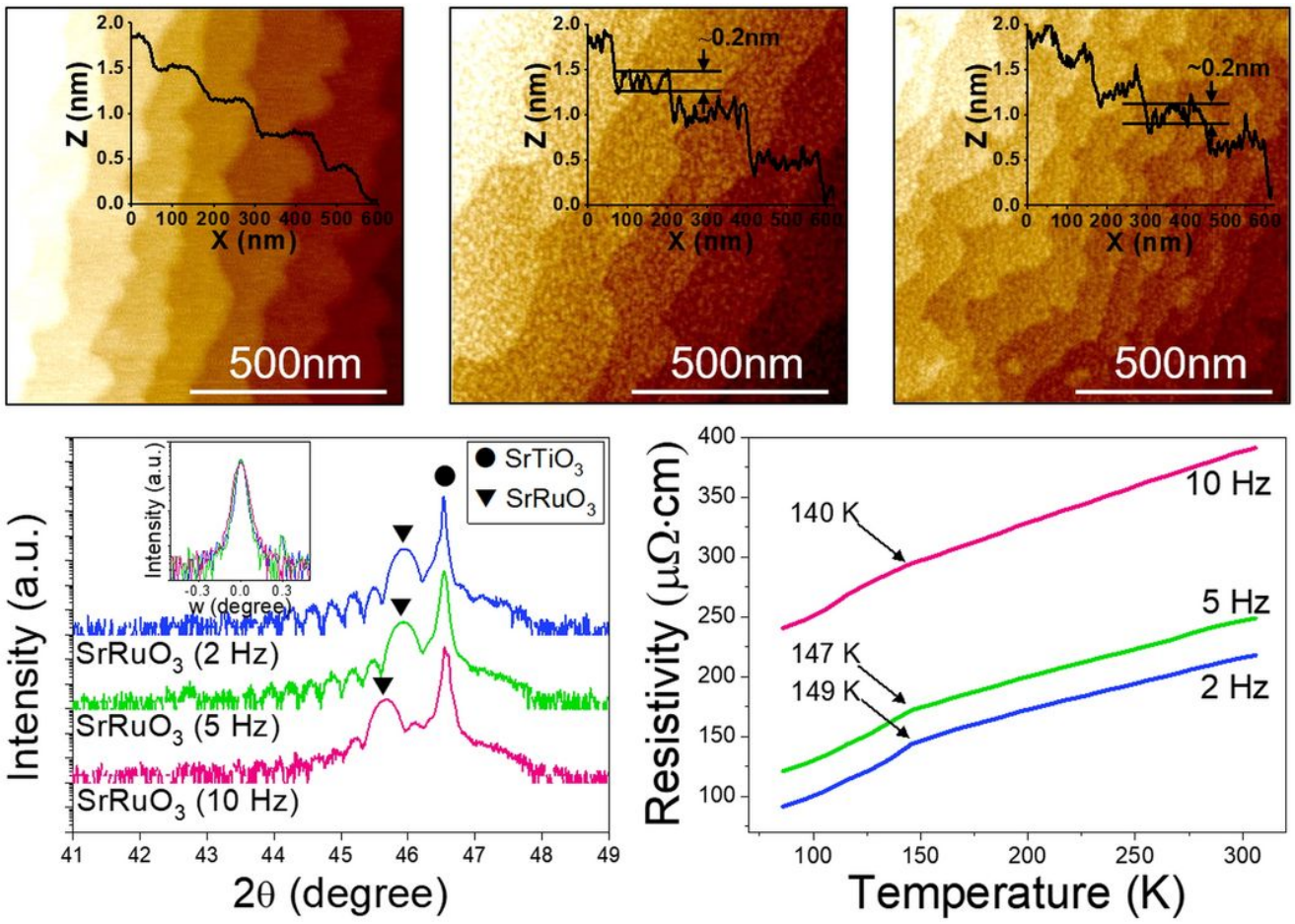


**Figure 1**

Structural characterization of $SrRuO_3$ bottom electrodes. (a–c) AFM images of $SrRuO_3$ electrodes grown at laser repetition frequencies of (a) 2, (b) 5, and (c) 10 Hz. (d) XRD patterns of $SrRuO_3$ electrodes; inset shows a rocking curve of the $SrRuO_3$ (200) peak. (e) Resistivity–temperature plots of the $SrRuO_3$ electrodes.

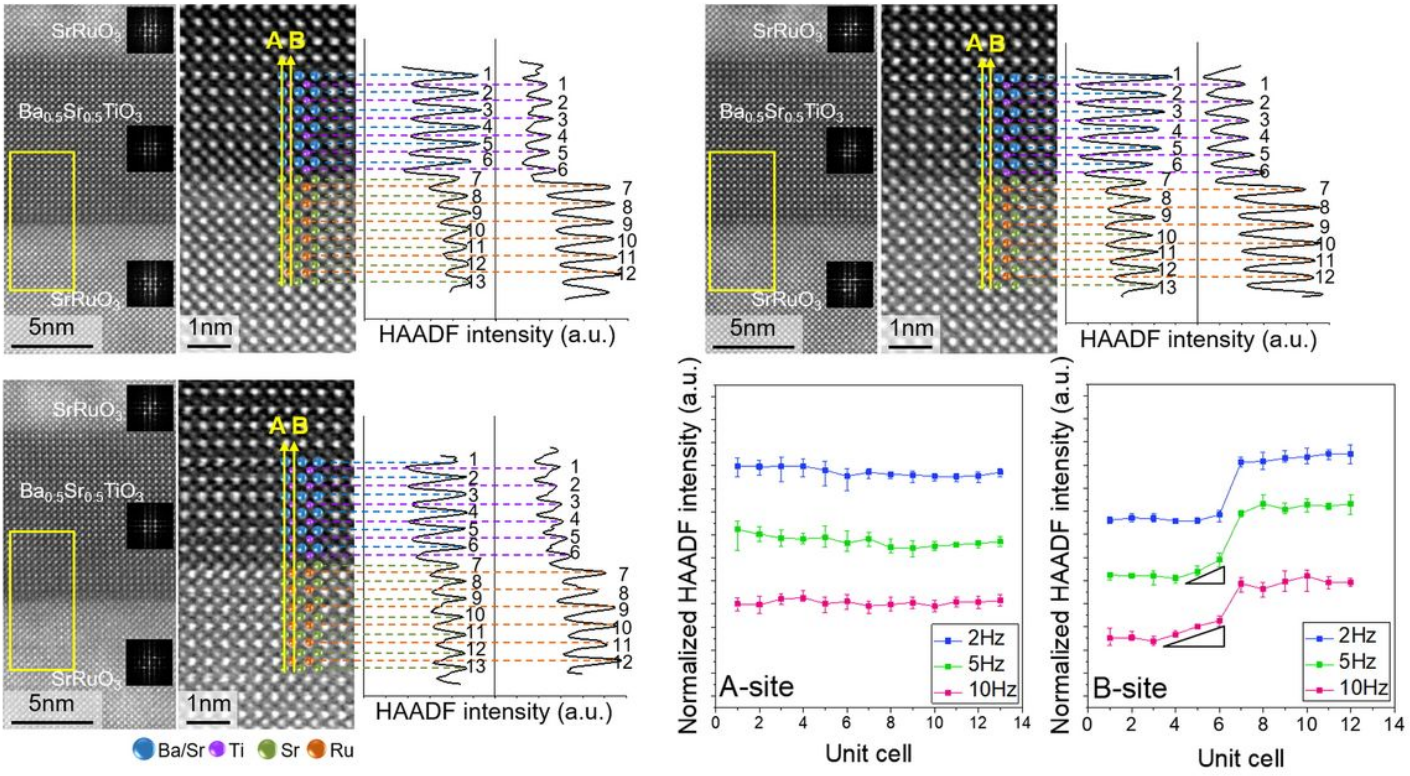


## Figure 2

Interface characterization of $SrRuO_3/Ba_{0.5}Sr_{0.5}TiO_3/SrRuO_3$ capacitor. (a, c, e) Cross-sectional HAADF-STEM images of capacitors with the $SrRuO_3$ electrodes grown at 2, 5, and 10 Hz, respectively; insets show the FFT pattern of each layer. (b, d, f) HAADF intensity profiles of sites A and B gathered from high-magnification HAADF-STEM images of the devices fabricated at 2, 5, and 10 Hz, respectively. (g) A- and (h) B-site peak intensities extracted from the HAADF intensity profiles as a function of the number of unit cells.

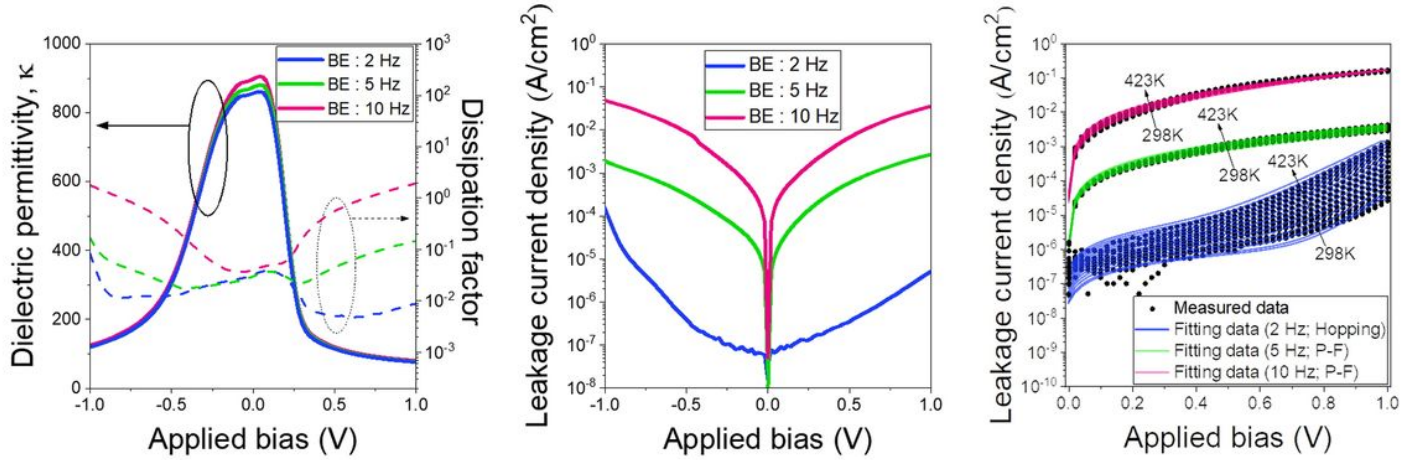


## Figure 3

Electrical properties of the $SrRuO_3/Ba_{0.5}Sr_{0.5}TiO_3/SrRuO_3$ capacitors. (a) Capacitance–voltage characteristics of each capacitor; dielectric permittivity and dissipation factors are represented by solid and dashed lines, respectively. (b) Current–voltage characteristics of each capacitor. (c) Current–voltage characteristics at different temperatures (298–423 K) and the corresponding fits based on different conduction mechanisms.

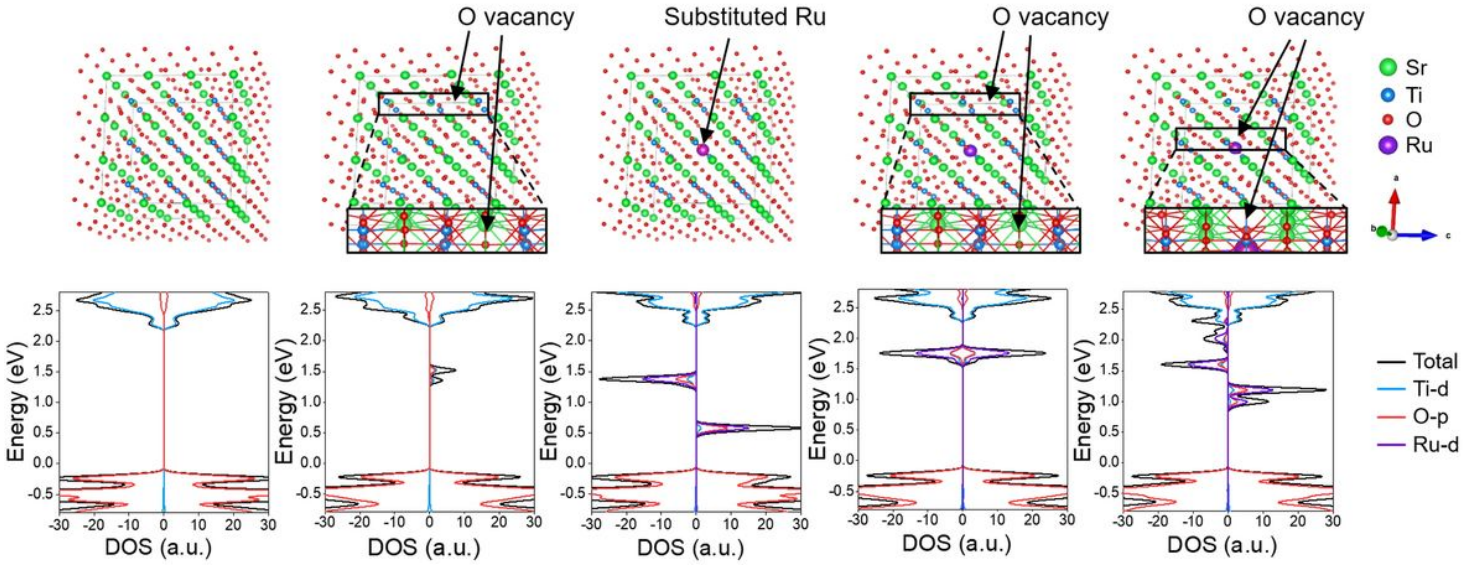


## Figure 4

Band structure predictions of $SrTiO_3$ according to various arrangements of substituted Ru and oxygen vacancy. Different structures in a 3 × 3 × 3 supercell with (a) any substituted Ru and oxygen vacancy, (b) one oxygen vacancy, (c) one substituted Ru, (e) one substituted Ru and one oxygen vacancy separated from each other, and (f) one substituted ruthenium adjacent to one oxygen vacancy. (f–j) Density of states corresponding to the aforementioned arrangements of substituted Ru and oxygen vacancy.

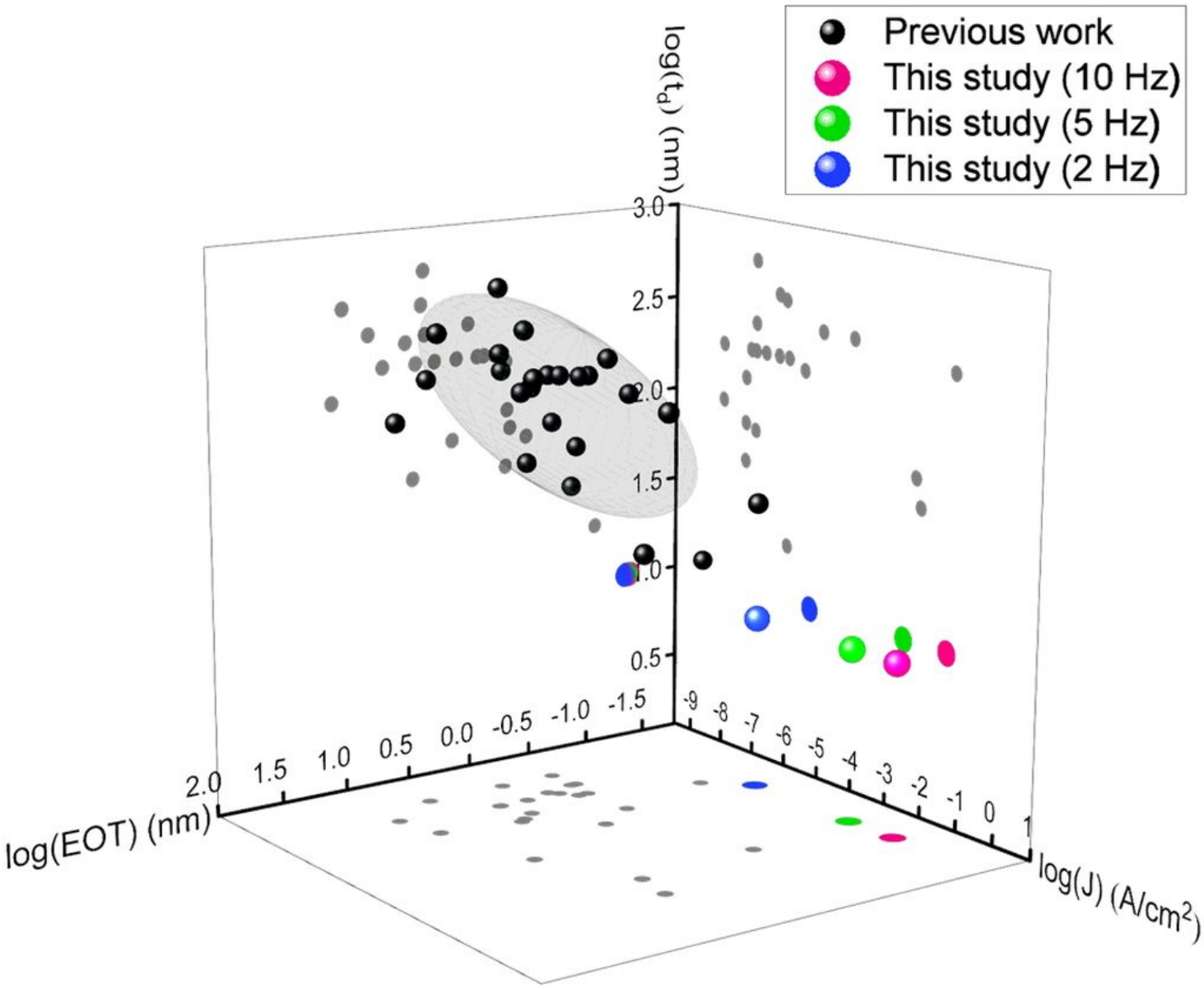


**Figure 5**

3D plots comparing the performance of capacitors that were previously developed and those reported herein: (a) equivalent oxide thickness versus thickness of dielectric layer, (b) leakage current density versus thickness of dielectric layer, and (c) equivalent oxide thickness versus leakage current density.

# Supplementary Files

This is a list of supplementary files associated with this preprint. Click to download.

- SupplementaryinformationNPGAsiaMaterialsJeongilBang.docx